Letter
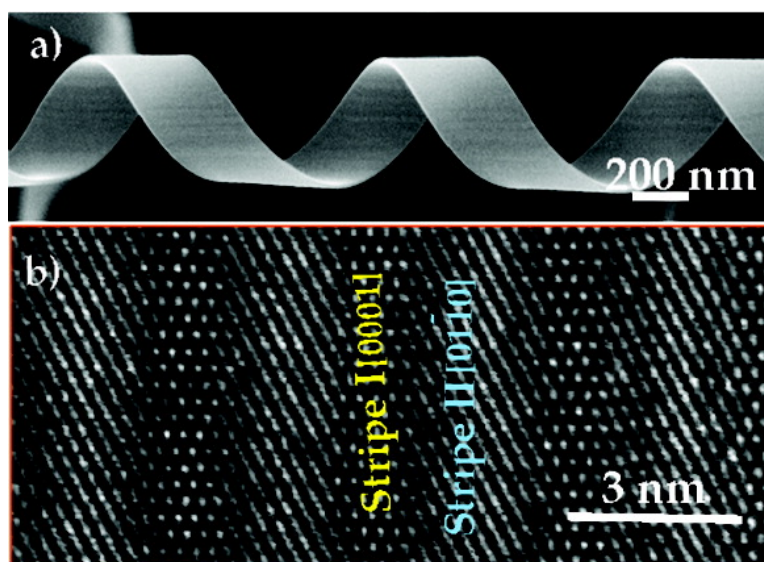
Electronic Transport in Superlattice-Structured ZnO Nanohelix

Pu-Xian Gao, Yong Ding, and Zhong Lin Wang

a) 200 nm

b) Stripe [0001] Stripe [0110] 3 nm

More About This Article

Additional resources and features associated with this article are available within the HTML version:

- Supporting Information
- Access to high resolution figures
- Links to articles and content related to this article
- Copyright permission to reproduce figures and/or text from this article

View the Full Text HTML

Electronic Transport in Superlattice-Structured ZnO Nanohelix

Pu-Xian Gao,*,†,‡ Yong Ding,‡ and Zhong Lin Wang*,‡

*Department of Chemical, Materials and Biomolecular Engineering & Institute of
Materials Science, University of Connecticut, Storrs, Connecticut 06269-3136, and
School of Materials Science and Engineering, Georgia Institute of Technology, Atlanta,
Georgia 30332-0245*

ABSTRACT

Superlattice-structured ZnO nanohelix is a structure that is made of a coiling nanobelt, which is composed of ZnO nanostripes oriented alternatively in two different orientations (*Science* 2005, *309*, 1700). The nanostripes run almost in parallel to the nanobelt direction but at an offset angle of ∼5°. We have measured the transport properties of a nanohelix and found its abnormal nonlinear characteristic. In comparison to the Ohmic transport property of a single crystal ZnO nanobelt measured under the same experimental conditions, the symmetric "Schottky-type" $I-V$ property of the nanohelix is suggested due to nanostripe boundaries and surfaces, where built-in periodic back-to-back energy barriers might occur across the nanostripe interfaces as a result of polar charges and interface-strain-induced piezoelectric effect. The effective potential barrier across the nanostripe boundary is estimated to be ∼24 meV. With the increasing of bias voltage, electrons can effectively tunnel through and thermionic emission across nanostripe boundaries, leading to a fast increase in transport current. It is suggested that the ZnO nanohelix could form a new type of band structure modulated superlattice for fabricating novel electronic devices.

In tuning the electronic and optical properties of semiconductors, surfaces, grain boundaries, and interfaces usually play very important roles. With the downscaling sizes of electronic and optoelectronic devices, the surfaces and interfaces become especially critical to their performance. For instance, as an important foundation of microelectronics, semiconductor superlattice heterostructures[1] are constructed with a controlled periodic electronic potential modulation by designed combination of dissimilar materials.[2] These traditional superlattices periodically modulate the electronic potential by dissimilar interfaces either with composition variation[3,4] or by doping-induced electrical field effect.[5−7] Such an artificial layering of multiphase or doped semiconductors has enabled a variety of functional devices with novel optical and electronic transport characteristics. Typical examples include resonant tunneling devices, lasers, photodiodes, and detectors.[8−10] In detail, important factors that determine the electronic transport properties of nanostructures include the dimensionality, composition, interface/surface structure, crystallinity, and the crystallographic orientation relating to some anisotropic parameters such as the piezoelectric effect and surface polar charges.

In this paper, electric transport along a superlattice structured nanohelix of ZnO has been characterized. An abnormal nonlinear electronic transport property is observed that is distinctly different from the linear characteristic of a single crystal nanobelt. The symmetric "Schottky-type" $I-V$ property of the nanohelix is suggested due to nanostripe boundaries and surfaces, where a built-in periodic back-to-back energy barrier modulation might occur across the nanostripe interfaces as a result of polar charges and strain-induced piezoelectric effect. This phenomenon is likely to reveal novel application of the nanohelices.

The superlattice structured nanohelices used for transport measurements were synthesized using a low vacuum vapor phase deposition process as described elsewhere.[11] The orientation-modulated superlattice is a helical structure by coiling a nanobelt, as illustrated in panels a and b of Figure 1. The nanohelix superlattice is about 300−800 nm in diameter, and the nanobelt is ∼10−30 nm in thickness and ∼100−600 nm in width. The observed superlattices lengths are in the range of ∼1−500 μm. The superlattice nanohelix is a periodic, coherent, epitaxial, and parallel assembly of two alternating stripes (S-I and S-II) of zinc oxide nanocrystals oriented with c axes perpendicular to each other (bottom inset in Figure 1b). Each nanostripe crystal has a width of ∼1.8 nm, defining a period of ∼3.5 nm. It is worth noting that ZnO has a wurtzite structure with cation Zn^{2+} and anions O^{2-} distributed in "layered structure" parallel to some crystal planes, such as (0001) and (01$\bar{1}$1), resulting in positively charged and negatively charged polar surfaces, respectively. This is the reason that many novel nanostruc-

* Corresponding authors: puxian.gao@ims.uconn.edu (P.X.G.); zhong.wang@mse.gatech.edu (Z.L.W.).
† University of Connecticut.
‡ Georgia Institute of Technology.
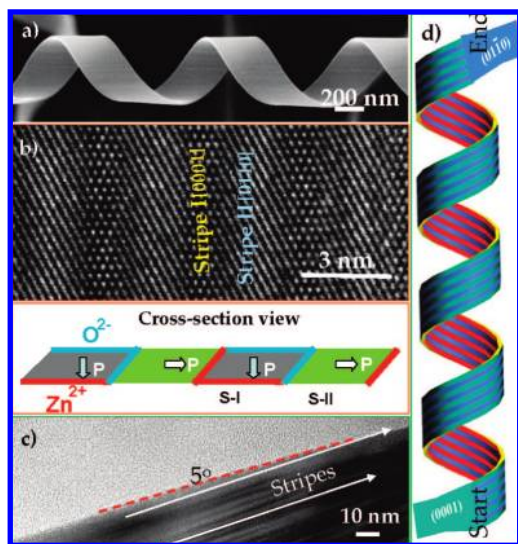
Figure 1. (a) SEM image of a right-handed nanohelix superlattice. (b) High-resolution transmission electron microscopy image recorded with the electron beam perpendicular to the surface of the nanobelt that coils to form the nanohelix, showing the superlattice structures. The nanostripes I and II are dominated by $\pm(0001)$ polar surfaces and $\pm\{01\bar{1}0\}$ nonpolar surfaces, respectively. The lower part is a schematic diagram of the nanobelt showing the cross section of the alternating nanostripes, where the polarizations introduced by polar charges in ZnO are indicated. (c) A $\sim5°$ offset angle is observed between the running directions of nanobelt and the nanostripes. (d) A schematic model of the structure of the nanohelix, in which the small offset angle of the nanostripes is not shown for clarity and easy illustration.

trures, such as nanorings and nanosprings have been fabricated for ZnO.[9,12]

The stripe S-I has top and bottom surfaces of $\pm(0001)$ polar surfaces, respectively; thus the dipole moment introduced by the surface polar charges for the strip is across the thickness direction (Figure 1c); stripe S-II has the $\pm\{01\bar{1}0\}$ nonpolar surfaces as its top and bottom surfaces, but with its polarization direction lying in the plane of the nanobelt (Figure 1c). Such a polarization introduces charges at the interface region between the strips.

The nanohelix growth starts with a structural transformation from a single-crystal $\pm(0001)$ dominated nanobelt into a $(01\bar{1}0)/(0001)$ superlattice structured nanohelix and then is terminated with a transformation into a $\pm\{01\bar{1}0\}$ dominated single-crystal nanobelt (as schemed in Figure 1d). It is suggested that reducing the polar surfaces could be the driving force for forming the superlattice structure, and the rigid structural rotation/twisting caused by the superlattice results in the initiation and formation of the nanohelix. The stripes in the nanobelt that forms the nanohelix run almost parallel to the direction of the nanobelt, but a small offset angle of $\sim5°$ has been found to exist between the direction of the stripes and that of the nanobelt, as shown in the transmission electron microscopy (TEM) image shown in Figure 1c.

To fabricate the three-dimensional (3D) nanohelix devices, photolithography (PL), electron-beam lithography (EBL), focused ion beam (FIB) lithography, together with standard etching and deposition technologies have been used. Three
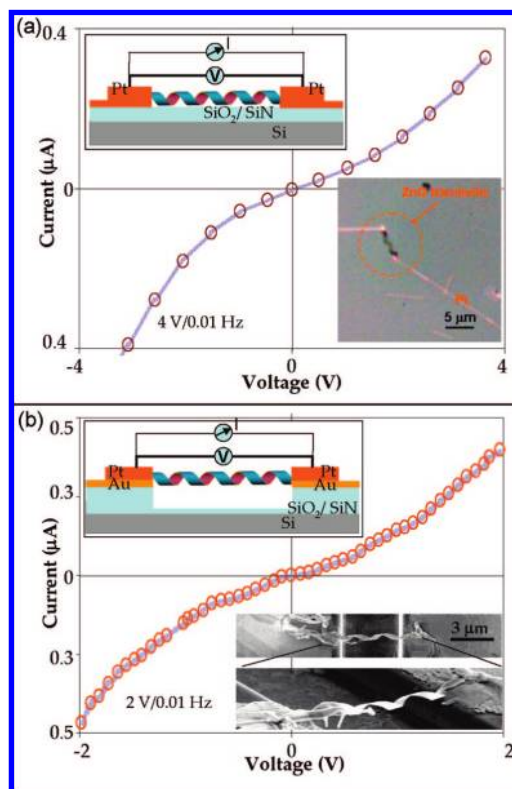

Figure 2. Typical room temperature current−voltage characteristics of two nanohelix devices measured for two different substrates configurations: (a) flat and (b) trenched SiO_2/Si_3N_4 substrates. The schemstic diagrams for the measurements and the corresponding SEM images of the fabricated devise are inset in the figure.

types of nanohelix device structures have been fabricated. To achieve good-enough contacts between the electrodes and nanohelices, we have chosen to make both ends of a nanohelix to be sandwiched by Au pads defined by PL or EBL, standard etching and deposition and Pt pads defined by FIB deposition. Careful switchings were manipulated between the secondary electron imaging mode and ion-beam deposition mode in the dual-beam FIB system during the FIB fabrication. By doing so, the Ga^{2+} ion beam induced Pt deposition has been limited only within the contact regions to avoid possible contamination of Pt over the entire nanohelix. For electrical characterization, both two-point and four-point probe methodologies have been used. To conduct the two-point probe measurement, a SRS DS345 synthesized functional generator and a Keithley 6485 5-1/2 digit picoammeter with 10fA resolution were used. A Keithley 6221 ac/dc current source and 2182A nanovoltmeter combination was used for the four-point probe current−voltage measurements. For both room and low temperature characterization, a VPF-700 LN2 optical cryostage was used as a vacuum chamber to hold the nanohelix devices. Au wire bonding and FIB nanolithography were used for ensuring good contact and interconnects between the nanohelix device and the test platform.

We have fabricated three different types of devices by choosing different substrate configurations and geometries. The insets in Figure 2a are the first type of devices we have fabricated. The device was fabricated following a process
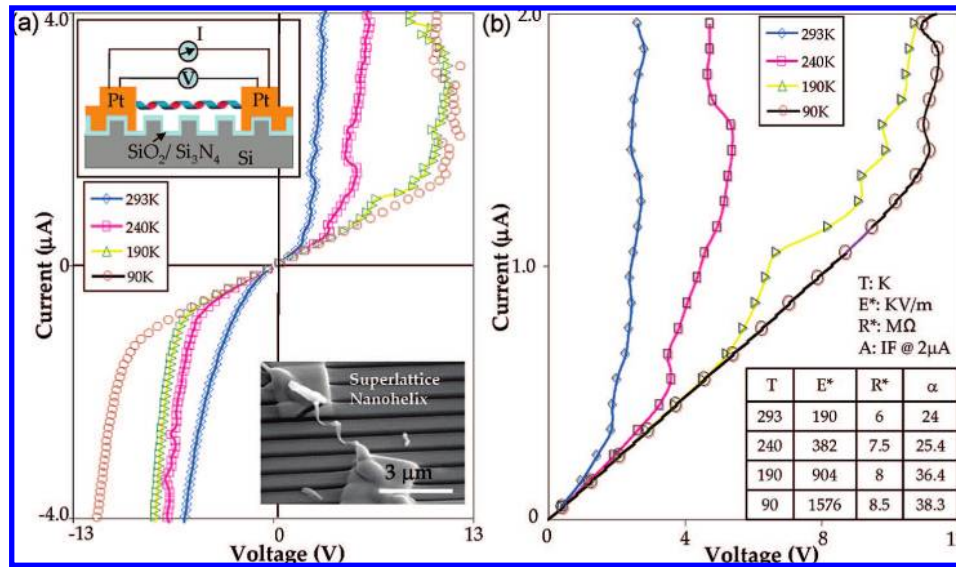
Figure 3. (a) A series of nonlinear $I-V$ curves of a ~4 μm long superlattice nanohelix measured at a temperature range of 293−90 K upon a current sweeping from −4 to +4 μA. (b) A 0 to 2 μA forward current sweeping $I-V$ curves of the device at different temperatures, showing different "breakdown strengths", "nonlinear ideal factors", and "low electric field resistances". The inset in (a) is the schematic diagram of the device. The inset table shows the evaluated parameters.

of nanohelices dispersing, locating, and FIB Pt deposition on flat SiO_2/Si_3N_4 insulated Si(100) substrate.[13] The Pt deposition was used to fix two ends of nanohelix and interconnect the device to the main contact pads prepatterned by PL or EBL. In this case, nanohelix directly contacted the SiO_2/Si_3N_4 insulated substrate. The bottom-right inset in Figure 2a is an optical image of an as-fabricated ZnO nanohelix device. Pt nanointerconnects with a width of ~200 nm and a thickness of 200 nm have been made by FIB-induced deposition to connect the as-deposited ZnO nanohelix ~5.6 μm long to blank two-terminal device microcontact electrodes for the two-point probe electrical characterization. The measurement was conducted by applying a slowly varying voltage bias of 2 V_{p-p} with a 0.01 Hz triangle waveform across the nanohelix. The insulating layer of SiO_2/Si_3N_4 ~1 μm thick has ensured a very large resistance of ~2 TΩ between the Si gate electrode and the two terminal Au electrodes. The current−voltage data were acquired by using Labview 7.0 after the nanohelix device circuit is loaded with bias for 30 s for electrically aging purpose. In Figure 2a, a typical $I-V$ curve of the nanohelix is shown, revealing a nonlinear characteristic in a voltage span of −2 to +2 V, similar to that in typically doped polycrystalline ZnO varistors. The linear characteristics of the $I-V$ curve in a low voltage range from −1 to 1 V, i.e., a low electrical field within 200 kV/m, indicated that the Ohmic law was obeyed; the resistance of the nanohelix is ~16 MΩ. But in the voltage span of 1−2 V, the curve becomes nonlinear with increasing conductivity with a resistance at 2 V being ~3 MΩ.

To eliminate a possible parasitic charging effect introduced by the substrate and the current leakage through the insulating layer, a nanohelix was suspended over a rectangular microtrench of ~5 μm in width and 5 μm in depth (Figure 2b). To fabricate this type of device, a nanomanipulator inside the FIB microscope has been used to locate, weld, and transfer a targeted nanohelix onto the finger electrodes

across the microtrench. A suspended nanohelix device in the bottom-right inset of Figure 2b has been tested using the two-point probe electrical measurement; a very similar nonlinear $I-V$ curve was obtained compared to that in Figure 2a.

Although a suspended nanohelix over the substrate in the second configuration (Figure 2b) works, the throughput is rather low with a relatively lengthy and inefficient nanomanipulation process involved. Therefore, a third configuration shown in Figure 3a seemed to be more practical and easy to accomplish. In this case, prepatterned SiO_2/Si_3N_4 insulated Si substrates with periodical microtrenches were used, where the nanohelices were dispersed across the microtrenches, and then FIB Pt deposition was used for fixing and interconnecting the devices with predefined microcontact pads.

To eliminate or reduce the contact resistance influence on the electrical characterization, a four-point probe characterization method is used to measure the $I-V$ characteristics of bare ZnO nanohelices, for which the typical results on a nanohelix device are shown in Figures 3 and 4. Similar nonlinear $I-V$ curves to the two-point probe characterization results in Figure 2 have been revealed. To further understand the nonlinear electronic transport property in ZnO nanohelix, temperature dependence electrical characterization was conducted. Figure 3a shows typical $I-V$ characteristics of a nanohelix ~4 μm in length, ~180 nm in width, ~20 nm in thickness, and ~400 nm in diameter (bottom right inset of Figure 3a), with the third device configuration (top left inset of Figure 3a) tested in a temperature range of room temperature 293−90 K. A current sweeping from −4 to 4 μA across the nanohelix has given rise to a series of nonlinear $I-V$ curves at 293, 240, 190, and 90 K. It is clearly seen that as the temperature decreases, the resistance of the ZnO nanohelix increases. The threshold voltage for transition from low electrical field linear transport region to high electrical field nonlinear transport region, i.e., the "break-down strength",
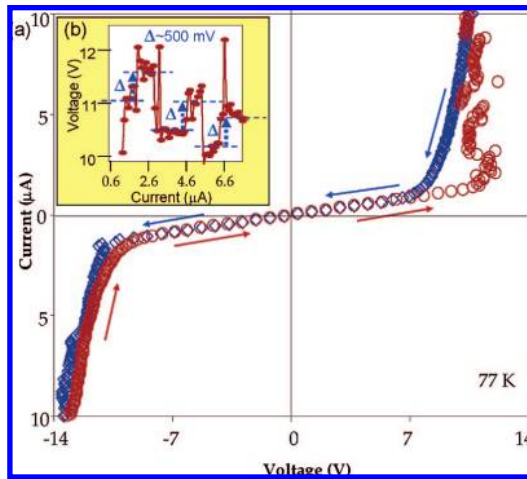
Figure 4. (a) Nonlinear $I-V$ characteristics of the ~ 4 μm long superlattice nanohelix measured in Figure 3 measured at 77 K in vacuum. (b) "Jumping steps" in voltage when the current was swept.

of the nanohelix increases as well. Specifically in the forward current sweeping region shown in Figure 3b, the "breakdown" strength increases from ~ 190 kV/m at room temperature to ~ 1600 kV/m at 90 K. At low field region, the resistance increase from ~ 6 MΩ to ~ 8.5 MΩ with the decreasing temperature. The nonlinear ideal factor (IF) at 2 μA was found to increase from ~ 24 to ~ 40 as the temperature decreased from 293 to 90 K, comparable to those in the bulk-doped ZnO varistors.[14] The table inset in Figure 3b listed the measured break-down strength, low-field resistance, and ideal factors at different temperatures. It is also found with a similar length, the wider the nanohelix has a smaller increase in "breakdown strength" with decreasing temperature. Due to a significant thermal electron tunneling suppression at 90 K compared to that at room temperature, the asymmetry level of the $I-V$ curves was reduced (Figure 3a).

In Figure 4a, a pair of typical 77 K current−voltage curves was shown for a large current forward and reverse sweeping in a range of ± 10 μA. Both forward and reverse sweepings give rise to consistent low field (less than 1.8 MV/m) linear $I-V$ characteristics, with a resistance of ~ 8.6 MΩ. While at a high field above 1.8 MV/m, it is found that the $I-V$ curve becomes highly nonlinear. The forward sweeping at forward high field led to a regular voltage oscillation (Figure 4b), with an amplitude of ~ 500 mV. The reverse sweeping at the reverse high field has shown a similar phenomenon but not as significant as the forward high field in the forward sweeping case, as observed in Figure 4b. It is worth noting that at room temperature no such voltage oscillation occurred. Therefore, a resonant tunneling of electrons at high field might happen with the large thermionic electron emission being suppressed at low temperature.

To explore the cause for the nonlinear behavior, several measures have been taken. First, the compliance of the current source in the four-point probe measurements was set at 40 V, much larger than the voltages of ~ 15 V used for transport measurements; furthermore, the two-point and four-point probe characterizations yielded results consistent with
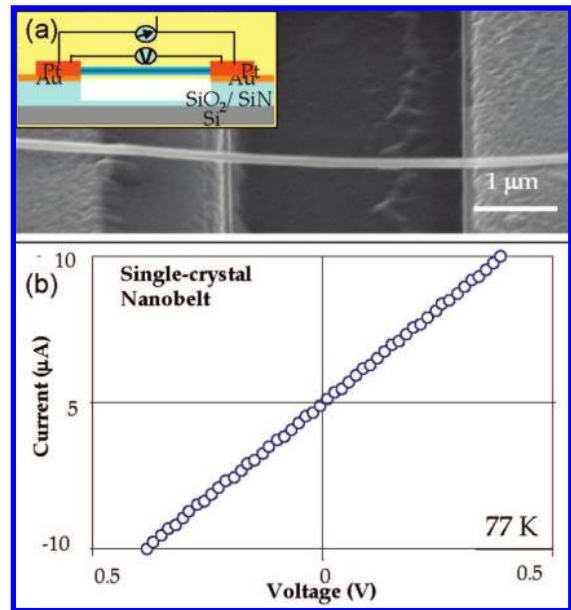

Figure 5. Transport property of a single-crystal ZnO nanobelt that was measured in a trenching configuration under the same conditions as prepared for the device shown in Figure 2b for the nanohelix. In contrast to the result shown in panel a, the nanobelt shows a linear transport property at 77 K in vacuum.

those illustrated in Figures 2−5; therefore the possible artifacts from instrumentations were eliminated. Second, both Pt/Au and Ag contact pads have been tried out in the device fabrication and testing; similar results have been yielded in the Ag Ohmic contact pads situation, which has eliminated the possible contribution from Schottky contact resistance.

To rule out the role played by contact in determining the nonlinear transport characteristic for the nanohelices, we have fabricated a device, as shown in Figure 5a, for measuring the transport properties of a single-crystal ZnO nanobelt following the same experimental procedure, electrode deposition, and measurements. The imaged nanobelt has a comparable dimensionality to the measured nanohelices used previously: ~ 150 nm in width, $\sim 20-30$ nm in thickness, and ~ 4 μm in length. In contrast, the nanobelt shows a linear Ohmic transport property (Figure 5b), similar to that in pure bulk polycrystalline ZnO.[15,16] This indicates that the nonlinear $I-V$ curve for the nanohelix is likely due to the intrinsic structure of the nanohelices. The nanobelt has a resistance of ~ 40 kΩ at 77 K. It is necessary to note that FIB deposited Pt usually has Ga impurity, which normally results in an Ohmic contact with ZnO although a pure Pt has Schottky contact with ZnO.[17]

With the exclusion of possible sources from the contact resistances and instrumentation, the nonlinear $I-V$ characteristic is likely due to the intrinsic property of superlattice nanostructures, i.e., by involving a periodically built-in electrostatic potential barrier across interfaces, which is elaborated in the following paragraphs.

Figure 6a plots the possible electron transport paths for the superlattice structured nanohelix with consideration that there is a small angle $\theta \sim 5°$ between the length direction of the strips and the nanobelt direction. When the length of
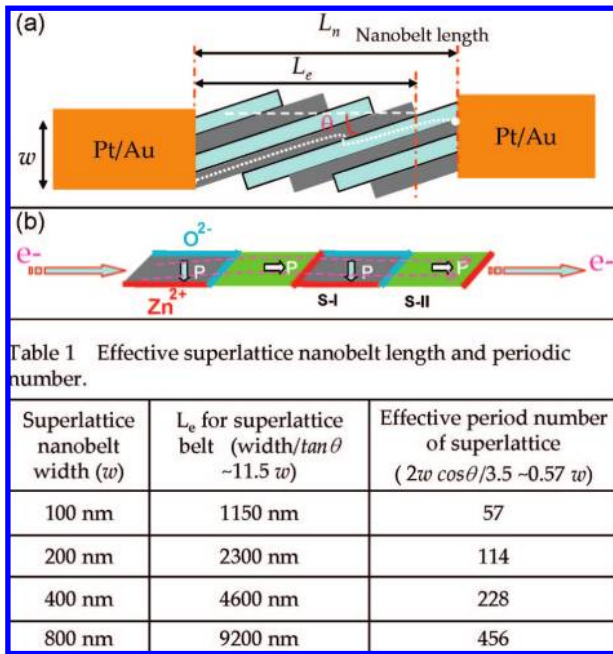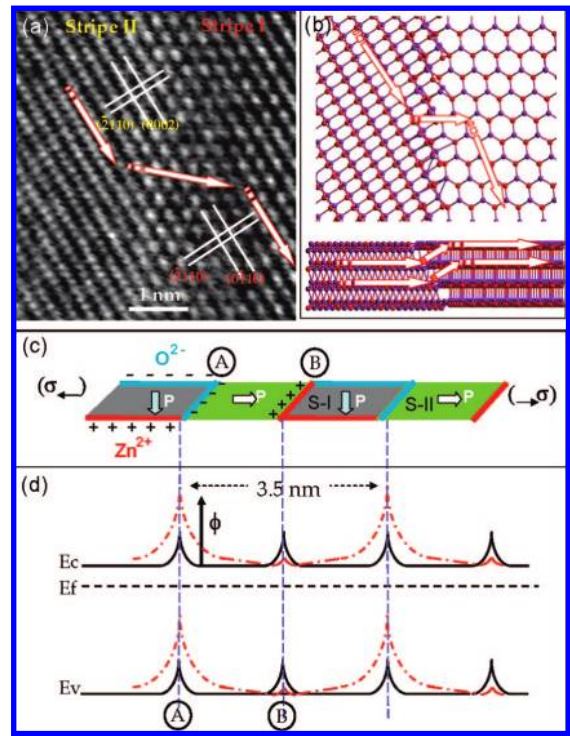
Figure 6. (a) A possible low-field electron flow pathway along the superlattice structured nanohelix provided the length of the running superlattice nanobelt between two Pt/Au electrodes is longer than the length of the nanostripe (b) A cross-section presentation of the electron pathways. The table lists the effective superlattice nanobelt length and number of superlattice nanostripes for the corresponding nanohelix.


Figure 7. (a) High-resolution transmission electron microscopy recorded with the electron beam perpendicular to the surface of the nanobelt, showing the interface structure between two nanostripes. A possible electron path is indicated. (b) Schematic atomic models showing the planar and cross-section structures between the two nanostripes. Possible electron paths are indicated. The cross-nanostripe boundary electron flow as well as the surface conduction from $\pm\{01\bar{1}0\}$ in nanostripe II to $\pm\{0001\}$ in nanostripe I (a) and (b). (c) Schematic diagram of ZnO superlattice nanostripe domains, corresponding polarization directions (P). (d) Internal stresses to illustrate the interface back-to-back potential-energy-barrier modulation in band structure due to the polar charges, anisotropic surface electronic structures, as well as piezoelectric effect, where the solid curve is the stress-free barrier profile and the dashed curve is the modified profile due to stress-induced polar charges.

the nanobelt exceeds $L_e = L_s \cos \theta$, where L_s is the total length of the stripe, as indicated in the plot, the electron has to pass through at least one boundary between two stripes before reaching the counter electrode.

Figure 6b gives a table listing the effective superlattice nanobelt length and the number of the superlattice nanostripes across the nanobelts for the several nanohelices whose $I-V$ property has been measured. It can be seen, for a $\sim$200 nm wide superlattice nanobelt, that the effective nanohelix length is $\sim$2.3 μm, which is significantly smaller than the 4 μm length of the measured nanohelix in Figure 4. For this nanohelix, $\sim$95 nanostripe boundaries were estimated to be passed across by electrons from one end to the other. At the breakdown voltage of $\sim$8.7 V, the applied voltage is estimated to be $\sim$91.6 mV per nanostripe boundary, much smaller than the typically 2−3 V/grain in bulk-doped ZnO varistors,[14] given that the nanostripe interfaces will be a major barrier for electron conduction here. This further confirmed that the nonlinear electrical transport of this nanohelix is attributed to the electron interaction with nanostripes, nanostripes boundaries, and nanoscale surfaces, where the existing periodically varying potentials across nanostripe interfaces would influence the local transport properties. This may be understood from the electric potential introduced by the polar charges.

First, highly anisotropic surfaces such as $\{0001\}$ and $\{01\bar{1}0\}$ in wurtzite-structured ZnO have significant potential (band structure) differences.[18] Figure 7a shows a possible electron transfer path across two adjacent nanostripes from II to I as indicated by a white arrowhead. Due to the

anisotropic crystal structure, the electron will transfer along the stacking direction of Zn and O ions, i.e., along $\langle 0001 \rangle$ directions[15,19] in the nanostripe II. At the same time, across the nanostripe interfaces, the surface paths as shown in the cross-section view of adjacent nanostripes I and II in Figure 7b will be important for the electron transport. The arrowheads in Figure 7b display the possible paths of electrons in the cross section of nanostripes. In the nanostripe II, electrons will flow through each column of Zn−O stacks along the c axis. When electrons pass through to the nanostripe I that is a polar nanostripe, they will follow the c axis first to reach the surfaces, and then the surface conductivity of $\langle 0001 \rangle$ will be another major source of the electron transport here.[15,19]

The nonlinear $I-V$ transport property of the nanohelix may be explained by considering the electrical potential introduced by polar charges from ZnO $\{0001\}$ planes and other polar surfaces as well as the stress-induced piezoelectric field[20−22] across oriented nanostripes. These factors might lead to significant electron depletion and trapping[23] to modify the potential barrier profile,[24] which therefore could form periodic
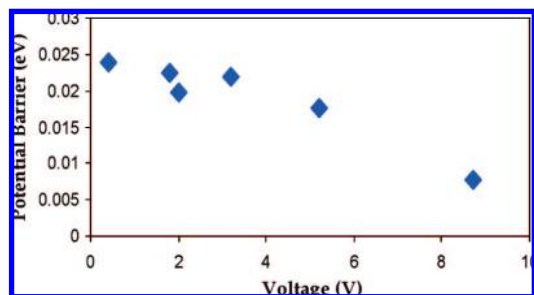
Figure 8. Effective potential energy barriers formed across the nanostripe interfaces under different voltage bias (electrical fields) derived based on the $I-V$ curves in Figure 3b.

back-to-back (double) Schottky barriers across the ZnO nanostripe boundaries, similar to that in the doped ZnO polycrystalline varistors involving thin insulating oxide layers around successive ZnO grains.[25] As shown in panels c and d of Figure 7, a possible potential-energy-barrier profile at zero bias can be introduced and modified by polar charges and the internal/external stresses σ induced by nanostripe lattice mismatch and external thermal or mechanical stimuli. With these 1.7 nm nanostripes, the back-to-back symmetric band bending at interface A is expected to overlap with the symmetric band bending at the interface B with overlapped depletion zones for these adjacent interfaces. In Figure 7d, the dark line indicates the conduction band with the existing of strain, and the red dashed line indicates the band energy level after considering the electric potential introduced by polar charges at the interfaces.

The potential barriers formed at the nanostripe interfaces strongly reduce the flow of charge carriers across the interface. Electrons have to be tunneling through and/or thermionic emit across the boundary, resulting in nonlinear $I-V$ characterisitic. Since the potential barrier is symmetric owing to the uniform periodicity of the superlattice stripes, a symmetric potential profile is created around the boundary. Therefore, the electron transport is symmetric. At low temperature, the thermionic emission was suppressed, so the tunneling effect induced by the superlattice nanostripe interfaces and anisostropic surfaces became significant, as evidenced by the regular ~500 mV voltage oscillations at high field forward current sweeping shown in Figure 4b.

To extract the potential barrier across the nanostripes, an approach similar to that for ZnO varistor grain boundaries was used.[26,27] When the temperature-dependent $I-V$ curves are replotted in logarithmic scale, i.e., $\mathrm{Ln}(I/T^2) \sim 1/T$ at intermediate voltages from 0.4 to 8.7 V in Figure 3b, the effective potential barriers formed across the nanostripes can be derived under the corresponding electrical fields as shown in Figure 8. The effective potential barriers for an electric field of 100 kV/m (0.4 V), 450 kV/m (1.8 V), 500 kV/m (2 V), and 1.3 MV/m (5.2 V) are calculated to be respectively ~23.9, ~22.5, ~19.7, and ~17.4 meV, with a decreasing trend. At a low temperature of 77 K, the estimated potential barrier will be as low as ~7.7 meV at a breakdown voltage of 8.7 V, which suggests the electrons can tunnel through the barrier easily, as evidenced by the breakdown and current oscillation that occurred at high field in Figure 4. It is worth pointing out that to sustain the periodically modulated back-to-back Schottky barriers (therefore the depletion layers) across the nanostripe boundaries, the anisotropic surface electronic structures as well as the different polar directions in nanostripes S-I and S-II are important factors, considering there is no insulation layer involved in the pure ZnO nanohelix superlattices, as proved by the high-resolution TEM image shown in Figures 1b and 7a.

In summary, a nonlinear current–voltage characteristic has been observed for superlattice structured ZnO nanohelix that is made of ZnO nanostripes oriented alternatively in two different orientations. The "breakdown" strength of a superlattice nanohelix increased from ~190 to ~1800 kV/m with the decreasing temperature from 293 to 77 K. The nonlinear ideal factor was found to increase from ~24 to ~40 with decreasing in temperature, comparable to those in the bulk-doped ZnO varistors. The nonlinear electronic transport behavior of nanohelix might be due to a major contribution from nanostripe boundaries and surfaces, where a built-in periodic back-to-back energy-barrier modulation might occur across the nanostripe interfaces as a result of polar charges and interface-strain-induced piezoelectric effect. The effective potential barrier across the nanostripe interface is estimated to be ~24 meV. With the increase of bias voltage, electrons can effectively tunnel and/or thermionic emission across nanostripe boundaries, leading to a fast increase in transport current. It is suggested that the nanohelix could form another new type of band structure modulated superlattice, which is in parallel to the traditional heterostructured superlattices created by chemical variation and/or doping modulation. It is suggested that the superlattice nanohelices with nonlinear electronic behaviors could be used as nanoscale nonlinear electronic devices in varistors,[28] lasers, sensors, and actuators. The nanohelix and its transport properties could also be potentially observed for wurtzite-structured materials such as ZnS, CdS, CdSe, AlN, InN, and GaN.

References
(1) (a) Esaki, L.; Tsu, R. *IBM J. Res. Dev.* **1970**, *14*, 61–65. (b) Esaki, L. In *Synthetic modulated structures*; Chang, L. L., Giessen, B. C., Eds.; Academic: New York, 1985; Chapter 1.
(2) Bjork, M. T.; Ohlsson, B. J.; Thelander, C.; Persson, A. I.; Deppert, K.; Wallenberg, L. R.; Samuelson, L. *Appl. Phys. Lett.* **2002**, *81*, 4458–4460.
(3) Ludeke, R.; Esaki, L.; Chang, L. L. *Appl. Phys. Lett.* **1974**, *24*, 417–419.
(4) Dingle, R.; Wiegmann, W.; Henry, C. H. *Phys. Rev. Lett.* **1974**, *33*, 827–830.
(5) Dohler, G. H. *Phys. Status Solidi* **1971**, *52* (79), 533. Dohler, G. H. *J. Vac. Sci. Technol.* **1979**, *16*, 851–856.
(6) Döhler, G. H.; Künzel, H.; Olego, D.; Ploog, K.; Ruden, P.; Stolz, H. J.; Abstreiter, G. *Phys. Rev. Lett.* **1981**, *47*, 864–867.
(7) Dohler, G. H. n-i-p-I doping superlattice-semiconductors with tunable electronic properties. In *The physics of submicron structures*; Grubin, H. L., Hess, K., Iafrate, G. J., Ferry, D. K., Eds.; Plenum Press: New York, 1984.
(8) Capasso, F. *Science* **1987**, *235*, 172–176.

(9) Li, Y.; Qian, F.; Xiang, J.; Lieber, C. M. *Mater. Today* **2006**, *9*, 18–27.

(10) Yang, C.; Barrelet, C. J.; Capasso, F.; Lieber, C. M. *Nano Lett.* **2006**, *6*, 2929–2934.

(11) Gao, P. X.; Ding, Y.; Mai, W.; Hughes, W. L.; Lao, C. S.; Wang, Z. L. *Science* **2005**, *309*, 1700–1704.

(12) (a) Kong, X. Y.; Wang, Z. L. *Nano Lett.* **2003**, *3*, 1625–1631. (b) Kong, X. Y.; Wang, Z. L. *Appl. Phys. Lett.* **2004**, *84*, 975–977. (c) Kong, X. Y.; Ding, Y.; Yang, R.; Wang, Z. L. *Science* **2004**, *303*, 1348–1351. (d) Yang, R.; Ding, Y.; Wang, Z. L. *Nano Lett.* **2004**, *4*, 1309–1312. (e) Hughes, W. L.; Wang, Z. L. *J. Am. Chem. Soc.* **2004**, *126*, 6703–6709. (f) Gao, P. X.; Wang, Z. L. *J. Appl. Phys.* **2005**, *97*, 044304. (g) Gao, P. X.; Wang, Z. L. *Small* **2005**, *1*, 722–726.

(13) Gao, P. X. Piezoelectric nanostructures of zinc oxide: synthesis, characterization and devices. Ph.D. dissertation, Georgia Institute of Technology, Atlanta, GA, December 2005.

(14) He, J. L.; Zeng, R.; Chen, Q. H.; Chen, S. M.; Guan, Z. C.; Han, S.-W.; Cho, H.-G. *IEEE Trans. Power Delivery* **2004**, *19*, 138–144.

(15) Sato, Y.; Oba, F.; Yamamoto, T.; Ikuhara, Y.; Sakuma, R. *J. Am. Ceram. Soc.* **2002**, *85* (8), 2142–2144.

(16) Oba, F.; Sato, Y.; Yamamoto, T.; Ikuhara, Y.; Sakuma, R. *J. Am. Ceram. Soc.* **2003**, *86* (9), 616–618.

(17) He, Jr. H. Unpublished results, 2008.

(18) Dulub, O.; Boatner, L. A.; Diebold, U. *Surf. Sci.* **2002**, *519*, 201–217.

(19) Sato, Y.; Tanaka, T.; Oba, F.; Yamamoto, T.; Ikuhara, Y.; Sakuma, T. *Sci. Technol. Adv. Mater.* **2003**, *4*, 605–611.

(20) Emtage, P. R. *J. Appl. Phys.* **1977**, *48* (10), 4372–4384.

(21) Clarke, D. R. *J. Am. Ceram. Soc.* **1999**, *82* (3), 485–502.

(22) Smith, D. L.; Mailhiot, C. *Rev. Mod. Phys.* **1990**, *62* (1), 173–234.

(23) Sato, Y.; Yamamoto, T. *J. Am. Ceram. Soc.* **2007**, *90* (2), 337–357.

(24) Verghese, P. M.; Clarke, D. R. *J. Appl. Phys.* **2000**, *87*, 4430–4438.

(25) Alim, M. A.; Seitz, M. A.; Hirthe, R. W. *J. Appl. Phys.* **1988**, *63*, 2337–2345.

(26) Levinson, L. M.; Philipp, H. R. *J. Appl. Phys.* **1975**, *46*, 1332–1341.

(27) Alim, M. A.; Li, S. T.; Liu, F. Y.; Cheng, P. F. *Phys. Status Solidi A* **2006**, *203*, 410–427.

(28) Gao, P.-X. provisional patent filed, University of Connecticut, 2008.

NL802682C